

# One-Compartment InGaN Nanowire Fuel Cell in the Light and Dark Operating Modes

Yongjie Chen, Hedong Chen, Jiaxun Song, Yingzhi Zhao, Lujia Rao, Guofu Zhou,\* and Richard Nötzel\*

Cite This: *ACS Omega* 2021, 6, 17464–17471

Read Online

ACCESS |



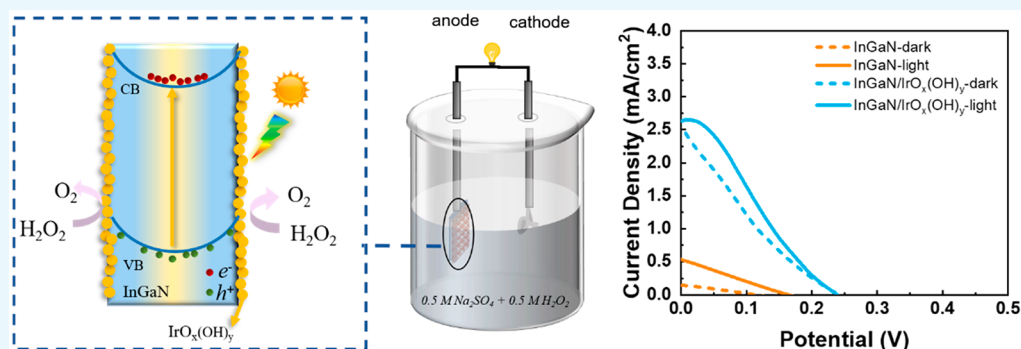
Metrics &amp; More



Article Recommendations



Supporting Information



**ABSTRACT:** A one-compartment H<sub>2</sub>O<sub>2</sub> photofuel cell (PFC) with a photoanode based on InGaN nanowires (NWs) is introduced for the first time. The electrocatalytic and photoelectrocatalytic properties of the InGaN NWs are studied in detail by cyclic voltammetry, current versus time measurements, photovoltage measurements, and electrochemical impedance spectroscopy. In parallel, IrO<sub>x</sub>(OH)<sub>y</sub> as the co-catalyst on the InGaN NWs is evaluated to boost the catalytic activity in the dark and light. For the PFC, Ag is the best as the cathode among Ag, Pt, and glassy carbon. The PFC operates in the dark as a conventional fuel cell (FC) and under illumination with 25% increased electrical power generation at room temperature. Such dual operation is unique, combining FC and PFC technologies for the most flexible use.

## 1. INTRODUCTION

Solar fuels will solve the severe problems of climate change and environmental pollution caused by the burning of fossil fuels.<sup>1,2</sup> A sustainable, clean solar energy cycle involves the production of solar fuels, the storage and transport, and the conversion to energy forms such as electricity or heat for use.<sup>3,4</sup> The production of hydrogen by photoelectrochemical water splitting in combination with fuel cells (FCs) for electricity generation is the most direct and advanced concept.<sup>5–8</sup> However, the realization of such an envisioned hydrogen economy currently faces difficulties with the hydrogen storage and transport, as well as safety concerns, which have to be solved. An immediate solution is hydrogen peroxide, H<sub>2</sub>O<sub>2</sub>, as the solar fuel.<sup>9–11</sup> Like hydrogen, it can be produced by photoelectrochemical oxidation of water or the reduction of oxygen gas; it has a comparable high energy density, a comparable redox potential, and remains liquid at room temperature for easy storage and transport. For the generation of electricity in FCs, only water and oxygen gas remain. Furthermore, H<sub>2</sub>O<sub>2</sub> has the huge advantage of allowing simple and cheap one-compartment FC designs without the need for membranes and different electrolytes. This is because H<sub>2</sub>O<sub>2</sub> acts as a fuel and, at the same time, as an electron acceptor or oxidant.<sup>12</sup> Such one-compartment FC realizations were so far

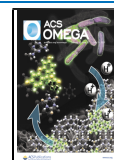
possible only for enzymatic bio-FCs, taking advantage of the high selectivity of enzyme catalysts for the oxidation of biological compounds which, however, sets free CO<sub>2</sub>.<sup>13–15</sup>

An advanced development in FC technology is the photofuel cell (PFC) which potentially provides high voltage and power due to the input of light. PFCs most commonly employ TiO<sub>2</sub> photoanodes and suitable metal cathodes.<sup>16–18</sup> However, due to the large band gap energy of TiO<sub>2</sub>, such PFCs only capture 5% of the solar energy in the ultraviolet spectral region. Other metal oxides under investigation are hampered by high carrier recombination rates and small carrier mobilities. In search for the best materials, InGaN is highly attractive. InGaN has a direct energy band gap which is tunable over the whole visible spectrum from the ultraviolet (GaN, 3.4 eV) to the near-infrared (InN, 0.7 eV) by the In content.<sup>19</sup> InGaN has a large absorption coefficient, a high carrier mobility,<sup>20,21</sup> and it is chemically very stable. InGaN, so far, has not been

Received: April 8, 2021

Accepted: June 17, 2021

Published: July 1, 2021



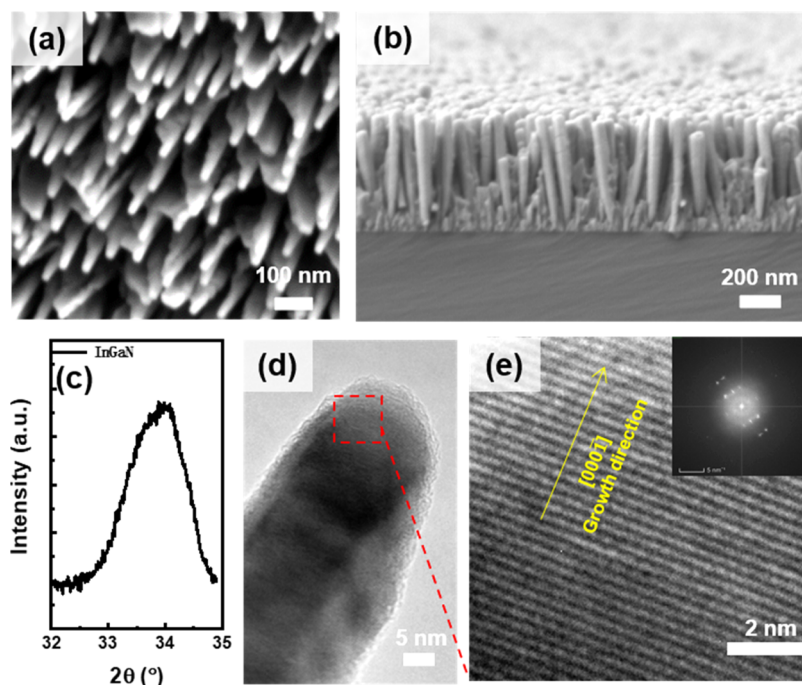


**Figure 1.** (a) Top-view SEM image and (b) cross-sectional SEM image of InGaN NWs on Si(111). (c) Omega-two-theta XRD spectrum in the vicinity of the (0002) InGaN Bragg reflection. (d) Cross-sectional TEM image and (e) high-resolution TEM image of an individual InGaN NW. Inset in (e) FFT of the high-resolution TEM image.

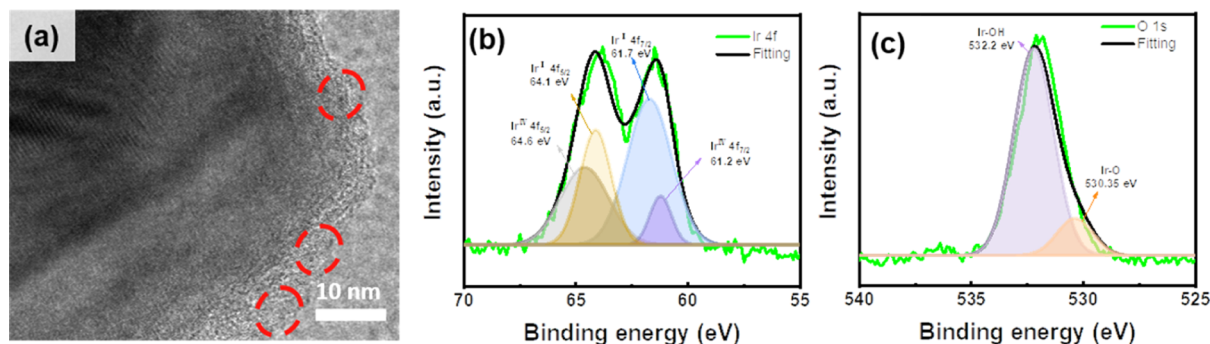


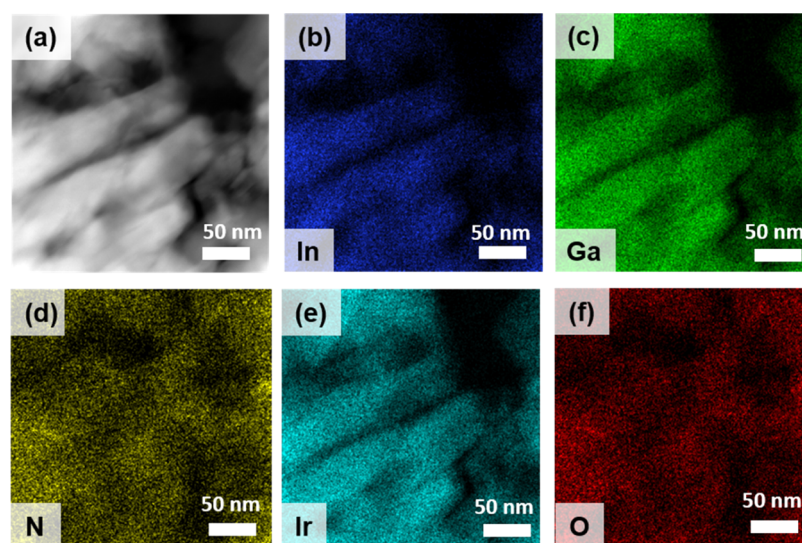
**Figure 2.** (a) Cross-sectional TEM image of an individual InGaN/IrO<sub>x</sub>(OH)<sub>y</sub> NW. The red circles indicate collections of IrO<sub>x</sub>(OH)<sub>y</sub> nanoparticles. (b,c) XPS spectra of the (b) Ir 4f region and the (c) O 1s region for the InGaN/IrO<sub>x</sub>(OH)<sub>y</sub> NWs.

implemented in PFCs. Moreover, strategies to boost the efficiency of photoelectrodes, such as surface modification by co-catalyst coupling,<sup>6,22,23</sup> heterostructuring,<sup>24–26</sup> and light management<sup>27–29</sup> are barely adopted in PFC technology.

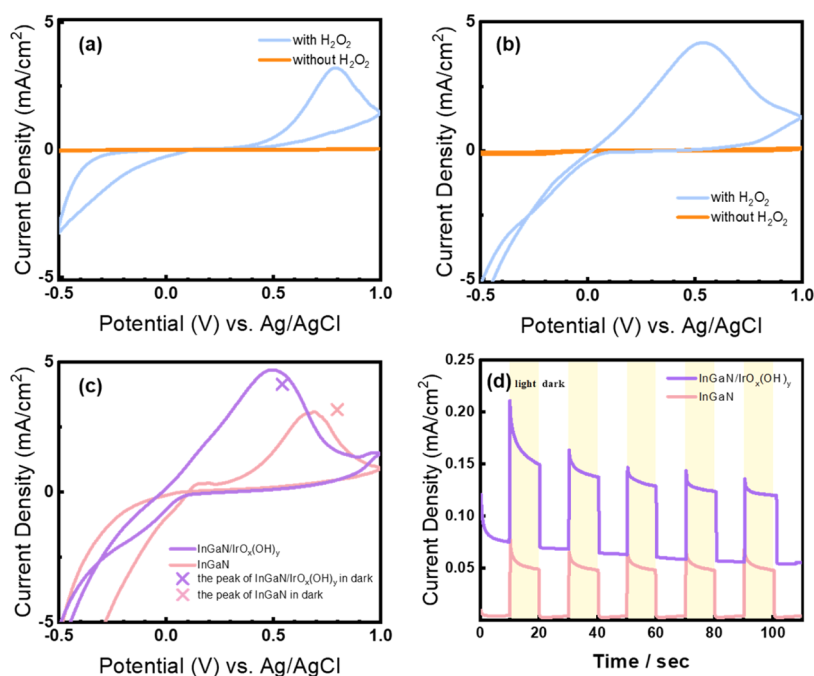
Here, we describe a one-compartment H<sub>2</sub>O<sub>2</sub> PFC with InGaN nanowires (NWs) as the photoanode and a Ag wire as the cathode. To boost the output power to competitive values, the InGaN NWs are decorated with IrO<sub>x</sub>(OH)<sub>y</sub> nanoparticles. IrO<sub>x</sub>(OH)<sub>y</sub> is an established, widely studied electrocatalyst for the oxygen evolution reaction of water.<sup>30,31</sup> The electrocatalytic and photoelectrocatalytic properties of the InGaN NW photoanode and InGaN/IrO(OH)<sub>y</sub> NW photoanode are studied in detail in the dark and light by cyclic voltammetry (CV), current density versus time (*I*–*t*) measurements, photovoltage versus time (PV–*t*) measurements, and electrochemical impedance spectroscopy (EIS). For the one-compartment H<sub>2</sub>O<sub>2</sub> PFC, Ag is identified to be the best cathode material among Ag, Pt, and glassy carbon (GC). The PFC operates in the light and also in the dark as conventional FC with high electrical output power at room temperature.

## 2. RESULTS AND DISCUSSION

**2.1. Structure.** Figure 1a,b shows the top-view scanning electron microscopy (SEM) image and cross-sectional SEM image of the InGaN NWs on a Si(111) substrate. Two-dimensional and three-dimensional atomic force microscopy (AFM) images of the NWs are presented in Figure S1. The average diameter and length of the NWs are 60 and 600 nm, respectively. The cross-section of the NWs is slightly elongated. The NWs are distributed discretely and uniformly with the NW axis oriented perpendicular to the substrate surface. An omega-two-theta X-ray diffraction (XRD) spectrum recorded around the InGaN(0002) Bragg reflection is shown in Figure 1c. An omega-two-theta XRD spectrum including the Si(111) reflection is shown in Figure S2. The InGaN(0002) reflection is centered at 16.95°, giving an In content of 22% by applying Bragg's law and Vegard's law:  $x_{(\text{In}_x\text{Ga}_{1-x}\text{N})} = (3.03)/\sin \theta_{(\text{In}_x\text{Ga}_{1-x}\text{N})} - 10.2$ .<sup>27</sup> Transmission electron microscopy (TEM) investigations, shown in Figure 1d,e, reveal well-resolved lattice fringes in the high-resolution



**Figure 3.** (a) Cross-sectional TEM image of InGaN/IrO<sub>x</sub>(OH)<sub>y</sub> NWs. (b–f) TEM–EDS element mappings of In, Ga, N, Ir, and O.



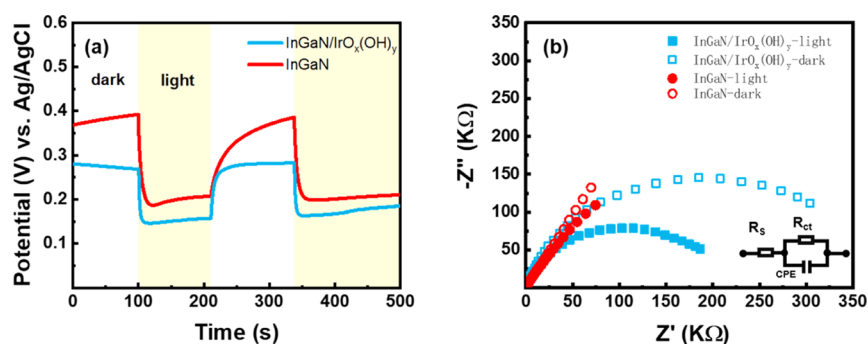
**Figure 4.** CV curves taken in 0.5 M H<sub>2</sub>O<sub>2</sub> and 0.5 M Na<sub>2</sub>SO<sub>4</sub> electrolyte for the (a) InGaN NWs and (b) InGaN/IrO<sub>x</sub>(OH)<sub>y</sub> NWs in the dark. CV curves without H<sub>2</sub>O<sub>2</sub> are shown for comparison. (c) CV curves of the InGaN NWs and InGaN/IrO<sub>x</sub>(OH)<sub>y</sub> NWs under 1 sun illumination. The CV scan rates are 50 mV/s. The crosses indicate the peak current densities in the dark from (a) and (b). (d) *I*–*t* curves of the InGaN NWs and InGaN/IrO<sub>x</sub>(OH)<sub>y</sub> NWs with 0.5 M H<sub>2</sub>O<sub>2</sub> and 0.5 M Na<sub>2</sub>SO<sub>4</sub> electrolyte at +0.6 V under chopped light with 10 s on–off cycles.

image in (e). The growth direction is along [0001], and the wurtzite crystal structure is confirmed from the fast Fourier transform (FFT) image of the high-resolution TEM image in the inset of (e).

After depositing the IrO<sub>x</sub>(OH)<sub>y</sub> co-catalyst, dense, amorphous nanoparticles with diameters of 2–5 nm<sup>32</sup> cover the InGaN NW surface, as visible in the TEM image in Figure 2a. Collections of nanoparticles are surrounded by the red circles. The X-ray photoelectron spectroscopy (XPS) spectra in Figure 2b,c confirm the nanoparticle compound as IrO<sub>x</sub>(OH)<sub>y</sub>. The four fitted peaks in the spectrum in the Ir 4f region in Figure 2b centered at 64.6, 61.7, 64.1, and 61.2 eV are ascribed to Ir<sup>IV</sup> 4f<sub>5/2</sub>, Ir<sup>IV</sup> 4f<sub>7/2</sub>, Ir<sup>I</sup> 4f<sub>5/2</sub>, and Ir<sup>I</sup> 4f<sub>7/2</sub>. In the spectrum in the O 1s region in Figure 2c, the fitted peak centered at 530.35 eV is

associated with the Ir–O bond. The fitted peak centered at 532.2 eV indicates the Ir–OH bond, which is established due to the IrO<sub>x</sub>(OH)<sub>y</sub> synthesis and electrochemical experiments in aqueous solutions.<sup>33,34</sup> In the XPS spectra of InGaN, there are no changes upon the deposition of IrO<sub>x</sub>(OH)<sub>y</sub>. Also, there are no changes during the photoelectrochemical oxygen evolution reaction, which has been confirmed before.<sup>27</sup>

The element distributions are deduced from energy dispersive X-ray spectroscopy (EDS) mappings in Figure 3 that are taken from the NWs shown in the cross-sectional TEM image in (a). The element distributions of In, Ga, N, Ir, and O in (b–f) coincide well, following the straight NW geometry. Naturally, the N and O distributions are more



**Figure 5.** (a) Open-circuit photovoltage of the InGaN NWs and InGaN/IrO<sub>x</sub>(OH)<sub>y</sub> NWs under light on–off cycles in 0.5 M H<sub>2</sub>O<sub>2</sub> and 0.5 M Na<sub>2</sub>SO<sub>4</sub> electrolyte. (b) EIS measurements at +0.4 V presented as Nyquist plots of the InGaN NWs and InGaN/IrO<sub>x</sub>(OH)<sub>y</sub> NWs in 0.5 M H<sub>2</sub>O<sub>2</sub> and 0.5 M Na<sub>2</sub>SO<sub>4</sub> electrolyte in the dark and light. Inset: Equivalent circuit. R<sub>ct</sub> denotes the charge transfer resistance, R<sub>s</sub> denotes the series resistance, and CPE denotes a constant phase element to account for the highly non-planar NW structure.

blurred. The IrO<sub>x</sub>(OH)<sub>y</sub> nanoparticles are evenly distributed on the surface of the InGaN NWs.

**2.2. Photoelectrocatalytic Activity of InGaN NWs and InGaN/IrO<sub>x</sub>(OH)<sub>y</sub> NWs.** The catalytic activity of the InGaN NW photoanode and InGaN/IrO<sub>x</sub>(OH)<sub>y</sub> NW photoanode toward the oxidation of H<sub>2</sub>O<sub>2</sub> is assessed in three-electrode configuration by CV and current density versus time (*I*–*t*) measurements. Figure 4a,b depicts the CV curves taken in the dark for the InGaN NWs and InGaN/IrO<sub>x</sub>(OH)<sub>y</sub> NWs in the presence of H<sub>2</sub>O<sub>2</sub>. The CV curves without H<sub>2</sub>O<sub>2</sub> are also shown. Pronounced oxidation peaks are revealed for both electrodes in the presence of H<sub>2</sub>O<sub>2</sub> which are absent without H<sub>2</sub>O<sub>2</sub>. Without H<sub>2</sub>O<sub>2</sub>, pure capacitive behavior is observed. This evidences the oxidation of H<sub>2</sub>O<sub>2</sub> rather than the oxidation of the electrodes. This is expected from the high chemical stability of InGaN, supported by the IrO<sub>x</sub>(OH)<sub>y</sub> co-catalyst. Compared to the InGaN NWs, the onset potential and peak potential for the oxidation of H<sub>2</sub>O<sub>2</sub> for the InGaN/IrO<sub>x</sub>(OH)<sub>y</sub> NWs are shifted by 0.2 and 0.25 V to lower values with respect to those for the InGaN NWs. The peak current density for the InGaN/IrO<sub>x</sub>(OH)<sub>y</sub> NWs is 150% larger than that for the InGaN NWs. This confirms that IrO<sub>x</sub>(OH)<sub>y</sub> is an efficient co-catalyst for the oxidation of H<sub>2</sub>O<sub>2</sub>. Notably, in the diffusion limited regime, for not too low scan rates, the peak current should not depend on the reaction rate, as described by the Randles–Sevcik equation. For this reason, in the CV curves for the InGaN NW photoanode and InGaN/IrO<sub>x</sub>(OH)<sub>y</sub> NW photoanode under 1 sun (AM 1.5, 100 mW cm<sup>-2</sup>) illumination, as shown in Figure 4c, the peak current densities are not changed much compared to those in the dark. However, the peak current voltages are clearly reduced. For better comparison, the peak current densities in the dark are indicated by crosses. In the presence of H<sub>2</sub>O<sub>2</sub>, the negative current densities in Figure 4a–c are caused by the reduction of H<sub>2</sub>O<sub>2</sub> at the InGaN electrode and oxidation of H<sub>2</sub>O<sub>2</sub> at the GC electrode for negative bias due to the easy reduction and oxidation reversal for H<sub>2</sub>O<sub>2</sub> under external bias.

The *I*–*t* measurements of the InGaN NWs and InGaN/IrO<sub>x</sub>(OH)<sub>y</sub> NWs measured at a constant voltage of +0.6 V (vs Ag/AgCl) under chopped 1 sun illumination are shown in Figure 4d. The photocurrent density for the InGaN/IrO<sub>x</sub>(OH)<sub>y</sub> NW photoanode, which is given by the current density under illumination minus the current density in the dark, is enhanced by up to 145% compared to that for the InGaN NW photoanode. The dark current density for the InGaN NWs is relatively low. The dark current density is

significantly higher for the InGaN/IrO<sub>x</sub>(OH)<sub>y</sub> NWs. The dark current density for the InGaN/IrO<sub>x</sub>(OH)<sub>y</sub> NWs is around half the photocurrent density. Hence, both the InGaN NWs and InGaN/IrO<sub>x</sub>(OH)<sub>y</sub> NWs reveal electrochemical activity in the dark, which is strongly enhanced under illumination and further boosted by the IrO<sub>x</sub>(OH)<sub>y</sub> co-catalyst. This corresponds to the voltage shifts in the CV measurements. The initial decay of the dark current density and photocurrent density after starting the measurement is due to the approach of equilibrium between the reaction of H<sub>2</sub>O<sub>2</sub> at the electrode surface and the diffusion of H<sub>2</sub>O<sub>2</sub> to the electrode surface. After that, the dark current density and photocurrent density are stable, confirming the chemical stability of the InGaN NWs and InGaN/IrO<sub>x</sub>(OH)<sub>y</sub> NWs. The chemical stability of InGaN against oxidation in aqueous solutions has been shown in our previous work. This stability is even improved by co-catalysts, promoting the oxidation of the target analyte rather than the oxidation of the electrode. For example, XPS spectra are unchanged after photoelectrochemical water splitting and the photocurrent density is stable over many hours.<sup>27</sup> However, in the case of H<sub>2</sub>O<sub>2</sub> oxidation, the adhesion of O<sub>2</sub> bubbles at the photoanodes leads to instability of the dark current density and photocurrent density after several minutes. Therefore, very long measurements cannot be performed. After removal of the bubbles, the dark current density and the photocurrent density are recovered.

For a complementary assessment of the electrochemical catalytic activity of the InGaN NWs and InGaN/IrO<sub>x</sub>(OH)<sub>y</sub> NWs, the photovoltage under open-circuit conditions for light on–off cycles is measured. Figure 5a presents the photovoltage and its transients in the photovoltage versus time (PV–*t*) measurements. The light off–on transient is due to the accumulation of photogenerated holes at the InGaN NW surface, screening the near-surface built-in electric field and, thus, reducing the near-surface upward energy band bending of the n-type InGaN NWs. The InGaN NWs are n-type because defects act as donors. Consequently, the photovoltage is negative. As expected, the light off–on transient is similar for both photoanodes as the built up of the hole surface accumulation is largely unaffected by the presence of the IrO<sub>x</sub>(OH)<sub>y</sub> co-catalyst. In contrast, for the light on–off transient, there is a marked difference. The light on–off transient is determined by the decay of the hole surface accumulation due to surface recombination and transfer of holes consumed in the H<sub>2</sub>O<sub>2</sub> oxidation reaction. As the IrO<sub>x</sub>(OH)<sub>y</sub> co-catalyst enhances the H<sub>2</sub>O<sub>2</sub> oxidation rate, as

revealed by the CV and  $I-t$  measurements, the on-off transient is much faster for the InGaN/IrO<sub>x</sub>(OH)<sub>y</sub> NW photoanode. This confirms the catalytic activity of IrO<sub>x</sub>(OH)<sub>y</sub> on the InGaN NWs.

The enhanced hole transfer for the InGaN/IrO<sub>x</sub>(OH)<sub>y</sub> NW photoanode is underlined by the EIS measurements performed in the dark and light at +0.4 V (vs Ag/AgCl) with H<sub>2</sub>O<sub>2</sub>. The Nyquist plots together with the equivalent circuit in the inset are shown in Figure 5b. The diameter of the semicircles gives the charge transfer resistance ( $R_{ct}$ ) which is reduced for the InGaN/IrO<sub>x</sub>(OH)<sub>y</sub> NW photoanode compared to that for the InGaN NW photoanode from about 420 to 240 KΩ in the dark. This confirms the enhanced charge transfer for H<sub>2</sub>O<sub>2</sub> oxidation in the presence of the IrO<sub>x</sub>(OH)<sub>y</sub> co-catalyst.<sup>35,36</sup>

**2.3. One-Compartment H<sub>2</sub>O<sub>2</sub> PFC.** One-compartment H<sub>2</sub>O<sub>2</sub> PFCs employing the InGaN NWs or InGaN/IrO<sub>x</sub>(OH)<sub>y</sub> NWs as the photoanode are constructed. Figure 6 illustrates

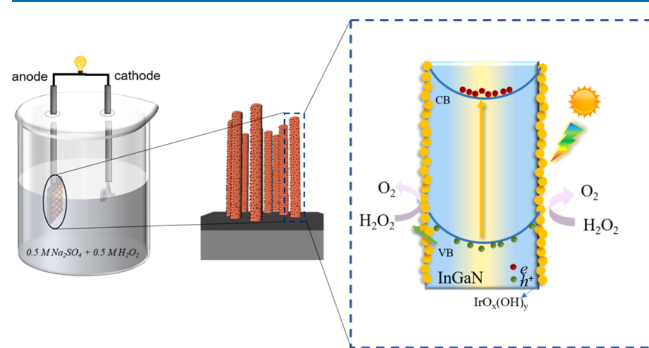
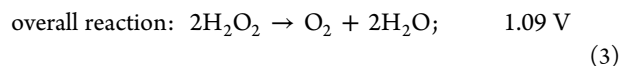
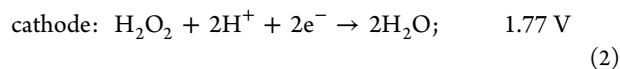
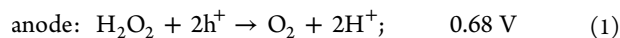


**Figure 6.** Schematic illustration of the H<sub>2</sub>O<sub>2</sub> PFC, the InGaN/IrO<sub>x</sub>(OH)<sub>y</sub> NW photoanode structure, and the reaction mechanism, including photocarrier generation, separation, transfer, and H<sub>2</sub>O<sub>2</sub> oxidation.

the scheme and working principle. The photoanode and cathode are immersed in the same electrolyte with H<sub>2</sub>O<sub>2</sub> for the anodic and cathodic reactions. There is no membrane separating the photoanode from the cathode. When light is incident on the photoanode, electrons and holes are photo-generated and separated due to the near-surface upward energy band bending in the InGaN NWs. The photogenerated holes are driven toward the electrode/electrolyte interface to oxidize H<sub>2</sub>O<sub>2</sub>. The photogenerated electrons are transferred to the cathode to reduce H<sub>2</sub>O<sub>2</sub>. The anodic and cathodic reactions read as follows<sup>37,38</sup>



H<sub>2</sub>O<sub>2</sub> acts as fuel which is oxidized at the anode and as the electron acceptor or oxidant which is reduced at the cathode. This allows the simple one-compartment PFC with only one electrolyte and no membranes.

For PFC performance, in addition to an efficient photoanode, the choice of the cathode material is crucial. In Figure 7a,b, the current density versus voltage ( $I-V$ ) measurements and deduced power density<sup>18</sup> versus voltage ( $P-V$ ) curves are compared for Ag, Pt, and GC employed as cathode materials. The InGaN NWs are the photoanode. The quasi-static scan

rate for taking the  $I-V$  curves is 10 mV/s. As a result, Ag performs best, exhibiting a high catalytic activity for the reduction of H<sub>2</sub>O<sub>2</sub>. In general, a H<sub>2</sub>O<sub>2</sub> FC generates power when the anode catalyst oxidizes H<sub>2</sub>O<sub>2</sub> at a more negative potential than the potential at which the cathode catalyst reduces H<sub>2</sub>O<sub>2</sub>. Therefore, to understand the superior performance of Ag, the Ag, Pt, and GC electrodes are characterized individually as working electrodes in a three-electrode configuration by CV with and without H<sub>2</sub>O<sub>2</sub>, shown in Figure S3. Ag exhibits the most positive onset potential for the reduction of H<sub>2</sub>O<sub>2</sub>, which has also been reported before.<sup>37</sup>

For demonstrating maximized PFC performance, Figure 7c,d depicts the  $I-V$  curves and corresponding  $P-V$  curves for the H<sub>2</sub>O<sub>2</sub> PFC constructed with the InGaN NW photoanode or InGaN/IrO<sub>x</sub>(OH)<sub>y</sub> NW photoanode and a Ag wire as the cathode. The  $I-V$  curves and  $P-V$  curves for the InGaN NW PFC show clear operation in the dark and light. In the dark, the performance is that of an ordinary one-compartment H<sub>2</sub>O<sub>2</sub> FC.<sup>37</sup> As mentioned, power is generated when selective oxidation of H<sub>2</sub>O<sub>2</sub> occurs at the anode at a lower potential in conjunction with selective reduction of H<sub>2</sub>O<sub>2</sub> at the cathode at a higher potential. Clearly, the InGaN NW anode with low reduction potential together with the catalytically highly active Ag cathode fulfill these conditions. However, the current densities and output power densities are relatively low. For the InGaN/IrO<sub>x</sub>(OH)<sub>y</sub> NW PFC, the current density, open circuit voltage, and power density in the dark amount to 2.5 mA cm<sup>-2</sup>, 0.24 V, and 0.12 mW cm<sup>-2</sup>, respectively. Under 1 sun illumination, the current density reaches 2.75 mA cm<sup>-2</sup>, the open circuit voltage reaches 0.24 V, and the maximum power density reaches 0.16 mW cm<sup>-2</sup>. This performance of the InGaN/IrO<sub>x</sub>(OH)<sub>y</sub> NW PFC under illumination is highly competitive with that of reported PFCs employing other photoanodes, which is summarized in Table 1.<sup>10-12,40</sup> The key feature of the InGaN/IrO<sub>x</sub>(OH)<sub>y</sub> NW PFC is the operation in both light and dark conditions with high output power. This, to the best of our knowledge, has not been reported by others. The PFC output power under illumination adds to the FC output power in the dark, providing high flexibility of operation. The  $I-V$  curves are stable over timescales of a few minutes. Then, the adhesion of O<sub>2</sub> bubbles due to H<sub>2</sub>O<sub>2</sub> decomposition at the electrodes leads to instability and current reduction, as discussed above. After removal of the bubbles, the  $I-V$  curves are recovered.

### 3. CONCLUSIONS

We have introduced a one-compartment H<sub>2</sub>O<sub>2</sub> PFC cell with a photoanode based on InGaN NWs for the first time. The NWs were coated with IrO<sub>x</sub>(OH)<sub>y</sub> nanoparticles acting as the co-catalyst. The electrocatalytic and photoelectrocatalytic properties of the InGaN NW photoanode and InGaN/IrO<sub>x</sub>(OH)<sub>y</sub> NW photoanode were studied by CV, current versus time measurements, photovoltage measurements, and EIS in the dark and light. For the cathode, Ag was found to be the best among Ag, Pt, and GC. The one-compartment H<sub>2</sub>O<sub>2</sub> PFC operates in the dark as conventional FC and under illumination with high electrical power generation. This dual operation is unique in combining electrocatalytic and photoelectrocatalytic FC and PFC technologies.

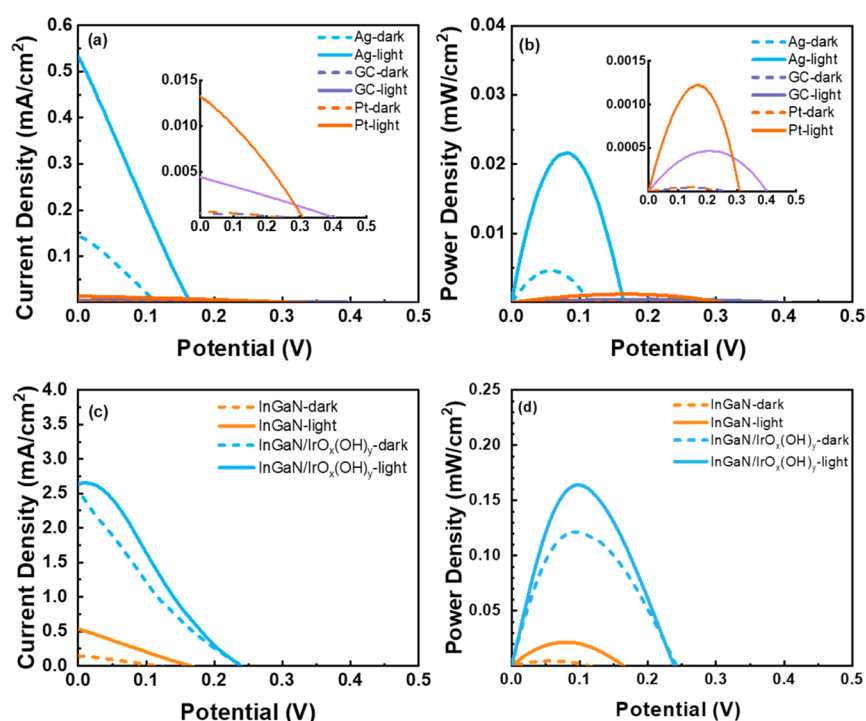


**Figure 7.** (a)  $I$ - $V$  curves and (b)  $P$ - $V$  curves of the  $\text{H}_2\text{O}_2$  PFCs with the InGaN NW photoanode and Ag, Pt, and GC cathodes under illumination and in the dark. In the insets in (a,b), the vertical scales are reduced. (c)  $I$ - $V$  curves and (d)  $P$ - $V$  curves of the  $\text{H}_2\text{O}_2$  PFCs with the InGaN NW photoanode or InGaN/ $\text{IrO}_x(\text{OH})_y$  NW photoanode and a Ag cathode under illumination and in the dark. The solution is 0.5 M  $\text{H}_2\text{O}_2$  and 0.5 M  $\text{Na}_2\text{SO}_4$  electrolyte.

**Table 1.** Performance Parameters of One-Compartment  $\text{H}_2\text{O}_2$  PFCs Taken from the Literature and This Work

samples	electrolyte	$J_{sc}/\text{mA cm}^{-2}$	$V_{oc}/\text{V}$	$P_{max}/\text{mW cm}^{-2}$	refs
$\text{TiO}_2/\text{FTO}$	0.1 M $\text{NaClO}_4$ and 0.1 M $\text{H}_2\text{O}_2$	0.197	0.607	0.0493	10
$\text{TiO}_2/\text{FTO}$	0.1 M $\text{NaClO}_4$ and 0.1 M $\text{H}_2\text{O}_2$	1.57	0.787		11
$\text{WO}_3$	seawater (containing ca. 48 mM $\text{H}_2\text{O}_2$ )		0.78	1.6	12
$\text{BiVO}_4/\text{FTO}$	0.1 M $\text{NaClO}_4$ and 0.1 M $\text{H}_2\text{O}_2$	0.81	0.61	0.13	40
Si/InGaN/ $\text{IrO}_x(\text{OH})_y$	0.5 M $\text{Na}_2\text{SO}_4$ and 0.5 M $\text{H}_2\text{O}_2$	2.75	0.24	0.16	this work

## 4. EXPERIMENTAL DETAILS

**4.1. Growth of InGaN NWs.** The InGaN NWs were grown on p-type Si(111) substrates by plasma-assisted molecular beam epitaxy (PA-MBE). The In and Ga metal fluxes were provided by standard Knudsen effusion cells. The active nitrogen species were generated with a radio frequency (RF) plasma source. The Si substrates were cleaned in 10 wt % HF aqueous solution for 1 min before loaded into the MBE chamber. After degassing in the MBE buffer chamber for 1 h at 300 °C, the Si substrates were transferred to the MBE growth chamber, annealed for 10 min at 900 °C (thermocouple reading) and nitrated in active N flux for 5 min to form a thin  $\text{SiN}_x$  layer. This  $\text{SiN}_x$  layer improves the InGaN crystal quality without introducing a significant electrical resistance to the well-conductive Si/InGaN interface junction.<sup>39</sup> For InGaN growth, the substrate temperature was 610 °C (thermocouple reading) with an In- and Ga beam equivalent pressure of  $7.6 \times 10^{-8}$  and  $1.32 \times 10^{-7}$  Torr, respectively. The active N RF source parameters were 350 W and 1.7 standard cubic centimeter per minute (sccm) molecular  $\text{N}_2$  flux rate. The growth time was 1 h.

**4.2. Synthesis of  $\text{IrO}_x(\text{OH})_y$  Co-catalyst Nanoparticles.** 0.01 g of  $\text{Na}_2\text{IrCl}_6 \cdot 6\text{H}_2\text{O}$  was slowly dissolved in 2 mL of 0.1 M aqueous NaOH solution with magnetic stirring until the

color of the solution turned amber. After cleaning with acetone, deionized water, ethanol and again water, the InGaN NW/Si samples were soaked into the  $\text{Na}_2\text{IrCl}_6/\text{NaOH}$  mixed solution for 1 h and dipped in deionized water for 30 s. The as-coated samples were dried at 80 °C for 15 min and further at 150 °C for 20 min in air. Then, the samples were annealed with the annealing temperature raised to 200 and to 300 °C within 100 min. The annealing was continued for 4 h at 300 °C before cooling down.<sup>32</sup> This preparation method does not allow a systematic change of the  $\text{IrO}_x(\text{OH})_y$  coverage. Attempts by varying the precursor concentration or rinsing time easily caused loss of the photoelectrocatalytic activity. Other co-catalysts have also been tried, including Pt and NiOOH.  $\text{IrO}_x(\text{OH})_y$  worked the best.

**4.3. Electrode Preparation.** The samples were coated with In-Ga eutectic on the back side of the substrate to form an ohmic contact and glued on a Cu conductive adhesive tape which was fixed on a supporting glass plate. The sample surface was then covered by non-transparent silicone rubber, leaving an opening for contact with the electrolyte.

**4.4. Materials Assessment.** The surface morphology and cross-section of the samples were investigated by field-emission SEM (FE-SEM; ZEISS Gemini 500) and AFM (Bruker MultiMode 8). XRD (PANalytical X'Pert PRO) was

performed using the Cu  $K\alpha_{1,2}$  radiations. Detailed structural characterization was by TEM (JEM-2100HR). XPS was conducted by an XPS spectrometer (EscaLab 250Xi). The XPS spectra were calibrated with respect to the C 1s peak. EDS element mappings were carried out with an EDS spectrometer (Aztec X-Max 80) attached to the TEM.

**4.5. Electrochemical Measurements.** The electrochemical measurements were performed using an electrochemical workstation (CHI 660E, Chenhua Instrument Co., Shanghai, China). A three-electrode photoelectrochemical cell was used to characterize the photoanodes and cathodes as working electrodes with a saturated KCl Ag/AgCl reference electrode and a GC counter electrode. The electrolyte was 0.5 M  $\text{Na}_2\text{SO}_4$  aqueous solution with and without 0.5 M  $\text{H}_2\text{O}_2$ . CV measurements were performed in the voltage range of  $-1$  to  $+1$  V versus Ag/AgCl with a scan rate 50 mV/s.  $I-t$  measurements at  $+0.6$  V versus Ag/AgCl were performed under chopped 10 s on–10 s off simulated sunlight (1 sun, AM 1.5, 100  $\text{mW cm}^{-2}$ , GLORIA-X500A).  $PV-t$  measurements were conducted in open-circuit configuration against Ag/AgCl, switching from dark to light and back. EIS measurements were taken in the frequency range of 10 Hz to 100 kHz in the dark and light. A two-electrode photoelectrochemical cell with the InGaN NWs or InGaN/ $\text{IrO}_x(\text{OH})_y$  NWs as the photoanode and a Ag wire, Pt mesh, or GC as the cathode, immersed in 0.5 M  $\text{Na}_2\text{SO}_4$  aqueous solution with 0.5 M  $\text{H}_2\text{O}_2$ , was constructed to evaluate the performance of the  $\text{H}_2\text{O}_2$  PFCs at room temperature.

## ■ ASSOCIATED CONTENT

### Supporting Information

The Supporting Information is available free of charge at <https://pubs.acs.org/doi/10.1021/acsomega.1c01844>.

AFM images and XRD spectrum of InGaN NWs on Si(111) and CV measurements with Ag, Pt, and GC working electrodes (PDF)

## ■ AUTHOR INFORMATION

### Corresponding Authors

**Richard Nötzel** – Guangdong Provincial Key Laboratory of Optical Information Materials and Technology, South China Academy of Advanced Optoelectronics, South China Normal University, Guangzhou 510006, People's Republic of China; National Center for International Research on Green Optoelectronics, South China Normal University, Guangzhou 510006, People's Republic of China; [orcid.org/0000-0003-2672-6363](https://orcid.org/0000-0003-2672-6363); Email: [richard.noetzel@scnu.edu.cn](mailto:richard.noetzel@scnu.edu.cn)

**Guofu Zhou** – Guangdong Provincial Key Laboratory of Optical Information Materials and Technology, South China Academy of Advanced Optoelectronics, South China Normal University, Guangzhou 510006, People's Republic of China; National Center for International Research on Green Optoelectronics, South China Normal University, Guangzhou 510006, People's Republic of China; Academy of Shenzhen Guohua Optoelectronics, Shenzhen 518110, People's Republic of China; [orcid.org/0000-0003-1101-1947](https://orcid.org/0000-0003-1101-1947); Email: [guofu.zhou@m.scnu.edu.cn](mailto:guofu.zhou@m.scnu.edu.cn)

### Authors

**Yongjie Chen** – Guangdong Provincial Key Laboratory of Optical Information Materials and Technology, South China Academy of Advanced Optoelectronics, South China Normal

University, Guangzhou 510006, People's Republic of China;

[orcid.org/0000-0002-8588-5631](https://orcid.org/0000-0002-8588-5631)

**Hedong Chen** – Guangdong Provincial Key Laboratory of Optical Information Materials and Technology, South China Academy of Advanced Optoelectronics, South China Normal University, Guangzhou 510006, People's Republic of China

**Jiaxun Song** – Guangdong Provincial Key Laboratory of Optical Information Materials and Technology, South China Academy of Advanced Optoelectronics, South China Normal University, Guangzhou 510006, People's Republic of China;

[orcid.org/0000-0002-9445-0429](https://orcid.org/0000-0002-9445-0429)

**Yingzhi Zhao** – Guangdong Provincial Key Laboratory of Optical Information Materials and Technology, South China Academy of Advanced Optoelectronics, South China Normal University, Guangzhou 510006, People's Republic of China;

[orcid.org/0000-0003-0553-9788](https://orcid.org/0000-0003-0553-9788)

**Lujia Rao** – Guangdong Provincial Key Laboratory of Optical Information Materials and Technology, South China Academy of Advanced Optoelectronics, South China Normal University, Guangzhou 510006, People's Republic of China;

[orcid.org/0000-0001-7452-2336](https://orcid.org/0000-0001-7452-2336)

Complete contact information is available at: <https://pubs.acs.org/doi/10.1021/acsomega.1c01844>

## Author Contributions

Y.C. performed the growth under supervision of R.N. Y.C. performed the measurements with support of H.C., J.S., and Y.Z. Y.C., G.Z., and R.N. discussed and interpreted the results. R.N. supervised the research and drafted the manuscript together with Y.C. All authors have discussed and commented on the manuscript. All authors have read and agreed to the published version of the manuscript.

## Notes

The authors declare no competing financial interest.

## ■ ACKNOWLEDGMENTS

This work was supported by: Program for Chang Jiang Scholars and Innovative Research Teams in Universities (no. IRT\_17R40), Science and Technology Program of Guangzhou (no. 2019050001), Guangdong Provincial Key Laboratory of Optical Information Materials and Technology (Grant no. 2017B030301007), and MOE International Laboratory for Optical Information Technologies and the 111 Project.

## ■ REFERENCES

- (1) Ma, Y.; Wang, X.; Jia, Y.; Chen, X.; Han, H.; Li, C. Titanium dioxide-based nanomaterials for photocatalytic fuel generations. *Chem. Rev.* **2014**, *114*, 9987–10043.
- (2) Chu, S.; Majumdar, A. Opportunities and challenges for a sustainable energy future. *Nature* **2012**, *488*, 294–303.
- (3) Tai, Q.; Tang, K.-C.; Yan, F. Recent progress of inorganic perovskite solar cells. *Energy Environ. Sci.* **2019**, *12*, 2375–2405.
- (4) Alvi, N. u. H.; Soto Rodriguez, P. E. D.; Aseev, P.; Gómez, V. J.; Alvi, A. u. H.; Hassan, W. u.; Willander, M.; Nötzel, R. InN/InGaIn quantum dot photoelectrode: Efficient hydrogen generation by water splitting at zero voltage. *Nano Energy* **2015**, *13*, 291–297.
- (5) Li, M.; Liu, Y.; Dong, L.; Shen, C.; Li, F.; Huang, M.; Ma, C.; Yang, B.; An, X.; Sand, W. Recent advances on photocatalytic fuel cell for environmental applications-The marriage of photocatalysis and fuel cells. *Sci. Total Environ.* **2019**, *668*, 966–978.
- (6) Liu, Z.; Song, Q.; Zhou, M.; Guo, Z.; Kang, J.; Yan, H. Synergistic enhancement of charge management and surface reaction kinetics by spatially separated cocatalysts and p-n heterojunctions in Pt/CuWO<sub>4</sub>/Co<sub>3</sub>O<sub>4</sub> photoanode. *Chem. Eng. J.* **2019**, *374*, 554–563.

- (7) Zhang, B.; Fan, W.; Yao, T.; Liao, S.; Li, A.; Li, D.; Liu, M.; Shi, J.; Liao, S.; Li, C. Design and Fabrication of a Dual-Photoelectrode Fuel Cell towards Cost-Effective Electricity Production from Biomass. *ChemSusChem* **2017**, *10*, 99–105.
- (8) Zhang, M.; Zhang, Z.; Xu, Y.; Wen, Z.; Ding, C.; Guo, Y.; Wang, K. A novel self-powered aptasensor for digoxin monitoring based on the dual-photoelectrode membrane/mediator-free photofuel cell. *Biosens. Bioelectron.* **2020**, *156*, 112135.
- (9) Yan, K.; Zhu, Y.; Ji, W.; Chen, F.; Zhang, J. Visible Light-Driven Membraneless Photocatalytic Fuel Cell toward Self-Powered Aptasensing of PCB77. *Anal. Chem.* **2018**, *90*, 9662–9666.
- (10) Masuda, T.; Fujishima, M.; Tada, H. Photo-effect on the electromotive force in two-compartment hydrogen peroxide-photofuel cell. *Electrochem. Commun.* **2018**, *93*, 31–34.
- (11) Akita, A.; Masuda, T.; Fujiwara, K.; Fujishima, M.; Tada, H. One-Compartment hydrogen peroxide-photofuel cell using TiO<sub>2</sub> photoanode and prussian blue cathode. *J. Electrochem. Soc.* **2018**, *165*, F300–F304.
- (12) Mase, K.; Yoneda, M.; Yamada, Y.; Fukuzumi, S. Seawater useable for production and consumption of hydrogen peroxide as a solar fuel. *Nat. Commun.* **2016**, *7*, 11470.
- (13) Santini, M.; Marzorati, S.; Fest-Santini, S.; Trasatti, S.; Cristiani, P. Carbonate scale deactivating the biocathode in a microbial fuel cell. *J. Power Sources* **2017**, *356*, 400–407.
- (14) So, K.; Kawai, S.; Hamano, Y.; Kitazumi, Y.; Shirai, O.; Hibi, M.; Ogawa, J.; Kano, K. Improvement of a direct electron transfer-type fructose/dioxygen biofuel cell with a substrate-modified biocathode. *Phys. Chem. Chem. Phys.* **2014**, *16*, 4823–4829.
- (15) Schievano, A.; Colombo, A.; Cossetti, A.; Goglio, A.; D'Ardes, V.; Trasatti, S.; Cristiani, P. Single-chamber microbial fuel cells as on-line shock-sensors for volatile fatty acids in anaerobic digesters. *Waste Manage.* **2018**, *71*, 785–791.
- (16) Lui, G.; Jiang, G.; Fowler, M.; Yu, A.; Chen, Z. A high performance wastewater-fed flow-photocatalytic fuel cell. *J. Power Sources* **2019**, *425*, 69–75.
- (17) Han, L.; Guo, S.; Wang, P.; Dong, S. Light-Driven, Membraneless, Hydrogen Peroxide Based Fuel Cells. *Adv. Energy Mater.* **2015**, *5*, 1400424.
- (18) Nishikiori, H.; Hashiguchi, S.; Ito, M.; Setiawan, R. A.; Fujii, T. Reaction in photofuel cells using allophane–titania nanocomposite electrodes. *Appl. Catal., B* **2014**, *147*, 246–250.
- (19) Moses, P. G.; Van de Walle, C. G. Band bowing and band alignment in InGa<sub>N</sub> alloys. *Appl. Phys. Lett.* **2010**, *96*, 021908.
- (20) Look, D. C.; Sizelove, J. R. Predicted maximum mobility in bulk GaN. *Appl. Phys. Lett.* **2001**, *79*, 1133.
- (21) Kaufmann, U.; Schlottter, P.; Obloh, H.; Köhler, K.; Maier, M. Hole conductivity and compensation in epitaxial GaN:Mg layers. *Phys. Rev. B: Condens. Matter Mater. Phys.* **2000**, *62*, 10867–10872.
- (22) Deng, X.; Tüysüz, H. Cobalt-Oxide-Based Materials as Water Oxidation Catalyst: Recent Progress and Challenges. *ACS Catal.* **2014**, *4*, 3701–3714.
- (23) Varadhan, P.; Fu, H.-C.; Priante, D.; Retamal, J. R. D.; Zhao, C.; Ebaid, M.; Ng, T. K.; Ajia, I.; Mitra, S.; Roqan, I. S.; Ooi, B. S.; He, J.-H. Surface Passivation of GaN Nanowires for Enhanced Photoelectrochemical Water-Splitting. *Nano Lett.* **2017**, *17*, 1520–1528.
- (24) Chang, X.; Wang, T.; Zhang, P.; Zhang, J.; Li, A.; Gong, J. Enhanced Surface Reaction Kinetics and Charge Separation of p-n Heterojunction Co<sub>3</sub>O<sub>4</sub>/BiVO<sub>4</sub> Photoanodes. *J. Am. Chem. Soc.* **2015**, *137*, 8356–8359.
- (25) Zhu, M.; Sun, Z.; Fujitsuka, M.; Majima, T. Z-Scheme Photocatalytic Water Splitting on a 2D Heterostructure of Black Phosphorus/Bismuth Vanadate Using Visible Light. *Angew. Chem., Int. Ed.* **2018**, *57*, 2160–2164.
- (26) Kumar, R.; Das, D.; Singh, A. K. C<sub>2</sub>N/WS<sub>2</sub> van der Waals type-II heterostructure as a promising water splitting photocatalyst. *J. Catal.* **2018**, *359*, 143–150.
- (27) Chen, H.; Wang, P.; Ye, H.; Yin, H.; Rao, L.; Luo, D.; Hou, X.; Zhou, G.; Nötzel, R. Vertically aligned InGa<sub>N</sub> nanowire arrays on pyramid textured Si (100): A 3D arrayed light trapping structure for photoelectrocatalytic water splitting. *Chem. Eng. J.* **2021**, *406*, 126757.
- (28) Ren, M.; Ao, Y.; Wang, P.; Wang, C. Construction of silver/graphitic-C<sub>3</sub>N<sub>4</sub>/bismuth tantalate Z-scheme photocatalyst with enhanced visible-light-driven performance for sulfamethoxazole degradation. *Chem. Eng. J.* **2019**, *378*, 122122.
- (29) Kimura, T.; Sato, S.; Kataoka, K.; Morikawa, T.; Nakamura, D. Self-Assembled Single-Crystalline GaN Having a Bimodal Meso/Macropore Structure To Enhance Photoabsorption and Photocatalytic Reactions. *ACS Appl. Mater. Interfaces* **2019**, *11*, 4233–4241.
- (30) Shan, J.; Guo, C.; Zhu, Y.; Chen, S.; Song, L.; Jaronec, M.; Zheng, Y.; Qiao, S.-Z. Charge-Redistribution-Enhanced Nanocrystalline Ru@IrO<sub>x</sub> Electrocatalysts for Oxygen Evolution in Acidic Media. *Chem* **2019**, *5*, 445–459.
- (31) Seitz, L. C.; Colin, F.; Dickens, K. N.; Hikita, Y.; Montoya, J.; Doyle, A.; Kirk, C.; Vojvodic, A.; Hwang, H. Y.; Norskov, J. K.; Jaramillo, T. F. A highly active and stable IrO<sub>x</sub>/SrIrO<sub>3</sub> catalyst for the oxygen evolution reaction. *Science* **2016**, *353*, 1011.
- (32) Chandra, D.; Takama, D.; Masaki, T.; Sato, T.; Abe, N.; Togashi, T.; Kurihara, M.; Saito, K.; Yui, T.; Yagi, M. Highly Efficient Electrocatalysis and Mechanistic Investigation of Intermediate IrO<sub>x</sub>(OH)<sub>y</sub> Nanoparticle Films for Water Oxidation. *ACS Catal.* **2016**, *6*, 3946–3954.
- (33) Kim, Y. I.; Hatfield, W. E. Electrical, magnetic and spectroscopic properties of tetrathiafulvalene charge-transfer compounds with iron, ruthenium, rhodium and iridium halides. *Inorg. Chim. Acta* **1991**, *188*, 15–24.
- (34) Li, J.; Pan, Z.; Zhou, K. Enhanced photocatalytic oxygen evolution activity by formation of Ir@IrO<sub>x</sub>(OH)<sub>y</sub> core-shell heterostructure. *Nanotechnology* **2018**, *29*, 405705.
- (35) Jia, J.; Sun, W.; Zhang, Q.; Zhang, X.; Hu, X.; Liu, E.; Fan, J. Inter-plane heterojunctions within 2D/2D FeSe<sub>2</sub>/g-C<sub>3</sub>N<sub>4</sub> nanosheet semiconductors for photocatalytic hydrogen generation. *Appl. Catal., B* **2020**, *261*, 118249.
- (36) Li, P.; Kong, L.; Liu, J.; Yan, J.; Liu, S. Photoassisted Hydrothermal Synthesis of IrO<sub>x</sub>-TiO<sub>2</sub> for Enhanced Water Oxidation. *ACS Sustainable Chem. Eng.* **2019**, *7*, 17941–17949.
- (37) Yamazaki, S.-i.; Siroma, Z.; Senoh, H.; Ioroi, T.; Fujiwara, N.; Yasuda, K. A fuel cell with selective electrocatalysts using hydrogen peroxide as both an electron acceptor and a fuel. *J. Power Sources* **2008**, *178*, 20–25.
- (38) Sanli, A. E.; Aytaç, A. Response to Disselkamp: Direct peroxide/peroxide fuel cell as a novel type fuel cell. *Int. J. Hydrogen Energy* **2011**, *36*, 869–875.
- (39) Wang, X.; Wang, P.; Yin, H.; Zhou, G.; Nötzel, R. An InGa<sub>N</sub>/SiN<sub>x</sub>/Si Uniband Diode. *J. Electron. Mater.* **2020**, *49*, 3577–3582.
- (40) Onishi, T.; Fujishima, M.; Tada, H. Solar-Driven One-Compartment Hydrogen Peroxide-Photofuel Cell Using Bismuth Vanadate Photoanode. *ACS Omega* **2018**, *3*, 12099–12105.